RESEARCH ARTICLE
PLANETARY SCIENCES

Earth and Planetary Physics
7: 371–377, 2023
doi: 10.26464/epp2023004

Ground calibration of the Mars orbiter magnetometer onboard Tianwen-1

ManMing Chen[1,2], Kai Liu[1,2*], XiaoWen Hu[1], YiRen Li[1,2], XinJun Hao[1,2], and ZongHao Pan[1,2]

[1]School of Earth and Space Sciences, University of Science and Technology of China, Hefei 230026, China;

[2]Chinese Academy of Sciences Center for Excellence in Comparative Planetology, University of Science and Technology of China, Hefei 230026, China

Key Points:

- The ground calibration of the Mars orbiter magnetometer sensors onboard the orbiter of Tianwen-1 determines all the calibration parameters and is thus one of the most important tasks prior to instrument delivery.
- The basic principle of ground calibration for the fluxgate magnetometer is described and calibration parameters are determined in a mathematical way.
- The results of the ground calibration showed that the magnetometer sensors are consistent with the design expectations and mission requirements and can be used for accurate measurements in orbit with the appropriate corrections.

Citation: Chen, M. M., Liu, K., Hu, X. W., Li, Y. R., Hao, X. J., and Pan, Z. H. (2023). Ground calibration of the Mars orbiter magnetometer onboard Tianwen-1. *Earth Planet. Phys.*, *7*(3), 371–377. http://doi.org/10.26464/epp2023004

Abstract: Ground calibration experiments of the Mars orbiter magnetometer (MOMAG) onboard the orbiter of Tianwen-1 were performed to determine the sensitivity, misalignment angle, and offset of the sensors. The linearity of the applied calibrated magnetic fields and the output from the sensors were confirmed to be better than 10^{-4}, and the sensor axes were orthogonal to each other within 0.5 degrees. The temperature dependencies of the sensitivity and misalignment angle were examined, but no clear signatures of temperature dependencies could be seen. Sensor offset and the stability of sensor offset drift with a temperature change were also determined by the rotation method. The stability of the sensor offset drift was less than 0.01 nT/°C. The ground calibration of MOMAG determines all the calibration parameters of the sensors for accurate magnetic field measurements in orbit with the appropriate corrections.

Keywords: Mars orbiter magnetometer; Tianwen-1; ground calibration

1. Introduction

Tianwen-1 is China's first Mars exploration; it consists of an orbiter, a lander, and a rover (Li CL et al., 2018, 2021). The Mars orbiter magnetometer (MOMAG) is one of seven scientific payloads onboard the orbiter. It is used to measure the magnetic field around the near-Mars space, from the solar wind to the magnetosheath and ionosphere (Li CL et al., 2021; Liu K et al., 2020). The MOMAG consists of two fluxgate magnetometer (FGM) sensors, an electronic box, and a deployable boom. The mission requirements for MOMAG are summarized in Table 1.

The FGM is the most widely used vector magnetometer for space magnetic field detection (Acuña, 2002), and the ground calibration is one of the most important tasks prior to instrument delivery (Risbo et al., 2003; Shimizu et al., 2008). It is essential to know the offsets, sensitivities, and misalignment angles of the fluxgate sensor beforehand to obtain accurate magnetic field data with the appropriate corrections. Furthermore, the temperature dependencies of the offset, sensitivity, and misalignment angle must be checked because the instruments (both the sensors and electronics) are often exposed to large temperature changes in orbit. The ground calibration can determine all the calibration parameters of the sensors for accurate magnetic field measurements (Auster et al., 2002; Russell et al., 2016; Cheng BJ et al., 2018) and can provide insights into the temperature dependencies of the calibration parameters (Nielsen et al., 1995; Magnes et al., 1998; Auster et al., 2008).

Unlike the in-flight calibration, which may be based on the properties of Alfvén waves (Wang GQ and Pan ZH, 2021a; Cheng SN et al., 2022; Hu XW et al., 2022a), mirror mode structures (Wang GQ and Pan ZH, 2021b; Hu XW et al., 2022b; Wang GQ, 2022), and current sheets (Wang GQ and Pan ZH, 2022), ground calibration of the FGM sensor must be conducted at specialized facilities that can generate the desired magnetic fields accurately in both strength and direction. The calibration facilities can also provide environments that are highly controlled, covering the full range of expected conditions in both temperature and field strength (Magnes et al., 1998; Auster et al., 2002; Risbo et al., 2003; Shimizu et al., 2008). However, the calibration schemes for different space-

First author: M. M. Chen, cmmshw@ustc.edu.cn
Correspondence to: K. Liu, kailiu@ustc.edu.cn
Received 29 JUN 2022; Accepted 21 SEP 2022.
Accepted article online 26 OCT 2022.
©2023 by Earth and Planetary Physics.

Table 1. Mission requirements for the Mars orbiter magnetometer.

Item	Requirements
Range	±2,000 nT (±10,000 nT for the dynamic field)
Linearity	better than 10^{-4}
Stability	≤0.01 nT/°C
Noise level	lower than 10 pT/$\sqrt{\text{Hz}}$ at 1 Hz
Sampling rate	1 Hz, 32 Hz, 128 Hz (optional)
Weight	≤5.6 kg
Power	≤3.9 W

based magnetometers are not identical. For example, the ground calibration of the SELENE lunar magnetometer followed the method of Yamamoto et al. (1996), in which multiple configurations between the magnetometer and the coil system were used to determine the relative directions of the sensors and the coil axes, with the help of cubic mirrors and a laser alignment system. Another typical ground calibration experiment was the preflight calibration mission of the Ørsted vector magnetometer, for which the "thin shell" method was developed. The calibration was conducted in the Magnetsrode coil system, which can automatically generate a sample of the coil setting vectors of the desired field strength and in uniformly distributed directions on the unit sphere, called spike spheres (Risbo et al., 2003).

For the MOMAG sensors, their sensitivities, misalignment angles, and dependencies on temperature change were determined in the Magnetsrode coil system, and the offsets and their dependencies on temperature change were calibrated in the low-field temperature test facility at the Magnetometer Laboratory of the Institut für Weltraumforschung (IWF, Graz, Austria) (Magnes et al., 1998; Auster et al., 2008). No tedious theodolite measurements were needed, nor was it necessary to establish any particular insert attitude of the sensor relative to the coil system.

In this article, we present the ground calibration of the MOMAG sensors. In Section 1, we give a brief introduction of the MOMAG mission and FGM ground calibration. The mathematical description of the ground calibration for the FGM is described in Section 2. The calibration of the sensitivities, misalignment angles, and offsets for the MOMAG sensors as well as their temperature dependencies are presented in Section 3. Finally, a summary of the ground calibration for the MOMAG sensors is given in Section 4.

2. Mathematical Description of the Calibration

2.1 Coordinate System

The raw output values of the magnetometer are expressed in the coordinate system $\boldsymbol{F}_w$ defined by the sensor mechanical axes, which are usually nonorthogonal with the basis $\{\boldsymbol{w}_1, \boldsymbol{w}_2, \boldsymbol{w}_3\}$. An ideal orthogonal sensor coordinate system $\boldsymbol{F}_u$ with the basis $\{\boldsymbol{u}_1, \boldsymbol{u}_2, \boldsymbol{u}_3\}$ is introduced to allow us to conveniently express the deviation between the mechanical axes of the sensor and the ideal orthogonal sensor coordinate system. The subscripts 1, 2, and 3 represent the three axes in the coordinate system, respectively. For the sake of generality, axis $\boldsymbol{u}_1$ is defined as being completely aligned with the sensor mechanical axis $\boldsymbol{w}_1$. Axis $\boldsymbol{u}_2$ lies in the plane defined by sensor mechanical axes $\boldsymbol{w}_1$ and $\boldsymbol{w}_2$, whereas $\boldsymbol{u}_3$ is defined as the cross product of axes $\boldsymbol{u}_1$ and $\boldsymbol{u}_2$, as shown in Figure 1a.

$$\begin{aligned} \boldsymbol{u}_1 &= \boldsymbol{w}_1, \\ \boldsymbol{u}_2 &= \boldsymbol{u}_3 \times \boldsymbol{w}_1, \\ \boldsymbol{u}_3 &= \frac{\boldsymbol{w}_1 \times \boldsymbol{w}_2}{|\boldsymbol{w}_1 \times \boldsymbol{w}_2|}. \end{aligned} \tag{1}$$

The relationship between $\boldsymbol{F}_w$ and $\boldsymbol{F}_u$ can be expressed as follows:

$$\begin{bmatrix} \boldsymbol{w}_1 \\ \boldsymbol{w}_2 \\ \boldsymbol{w}_3 \end{bmatrix} = \begin{bmatrix} 1 & 0 & 0 \\ \sin\alpha & \cos\alpha & 0 \\ \sin\theta & \cos\theta\cos\beta & \cos\theta\sin\beta \end{bmatrix} \begin{bmatrix} \boldsymbol{u}_1 \\ \boldsymbol{u}_2 \\ \boldsymbol{u}_3 \end{bmatrix} = \boldsymbol{T} \begin{bmatrix} \boldsymbol{u}_1 \\ \boldsymbol{u}_2 \\ \boldsymbol{u}_3 \end{bmatrix}. \tag{2}$$

The angles (ξ_{12}, ξ_{23}, and ξ_{13}) between the sensor mechanical axes, as presented in Figure 1b, can then be expressed as

$$\begin{aligned} \cos\xi_{12} &= \boldsymbol{w}_1 \cdot \boldsymbol{w}_2 = \sin\alpha, \\ \cos\xi_{23} &= \boldsymbol{w}_2 \cdot \boldsymbol{w}_3 = \sin\alpha\sin\theta + \cos\alpha\cos\beta\cos\theta, \\ \cos\xi_{13} &= \boldsymbol{w}_1 \cdot \boldsymbol{w}_3 = \sin\theta. \end{aligned} \tag{3}$$

A vector magnetic field $\boldsymbol{B}$ can be expressed in the two coordinate systems as follows:

$$\boldsymbol{B} = \begin{bmatrix} B_{w_1} B_{w_2} B_{w_3} \end{bmatrix} \begin{bmatrix} \boldsymbol{w}_1 \\ \boldsymbol{w}_2 \\ \boldsymbol{w}_3 \end{bmatrix} = \begin{bmatrix} B_{u_1} B_{u_2} B_{u_3} \end{bmatrix} \begin{bmatrix} \boldsymbol{u}_1 \\ \boldsymbol{u}_2 \\ \boldsymbol{u}_3 \end{bmatrix}. \tag{4}$$

Thus, the three components of $\boldsymbol{B}$ in the orthogonal coordinate system $\boldsymbol{F}_u$ can be expressed as

$$\begin{bmatrix} B_{u_1} \\ B_{u_2} \\ B_{u_3} \end{bmatrix} = \boldsymbol{T}^{\mathrm{T}} \begin{bmatrix} B_{w_1} \\ B_{w_2} \\ B_{w_3} \end{bmatrix} = \begin{bmatrix} 1 & \sin\alpha & \sin\theta \\ 0 & \cos\alpha & \cos\theta\cos\beta \\ 0 & 0 & \cos\theta\sin\beta \end{bmatrix} \begin{bmatrix} B_{w_1} \\ B_{w_2} \\ B_{w_3} \end{bmatrix}. \tag{5}$$

According to Equation (3), $\boldsymbol{T}^{\mathrm{T}}$ can be expressed with angles ξ_{12}, ξ_{23}, and ξ_{13} as follows:

$$\boldsymbol{T}^{\mathrm{T}} = \begin{bmatrix} 1 & \cos\xi_{12} & \cos\xi_{13} \\ 0 & \sin\xi_{12} & \dfrac{\cos\xi_{23} - \cos\xi_{12}\cos\xi_{13}}{\sin\xi_{12}} \\ 0 & 0 & \sqrt{\sin^2\xi_{13} - \dfrac{(\cos\xi_{23} - \cos\xi_{12}\cos\xi_{13})^2}{\sin^2\xi_{12}}} \end{bmatrix}. \tag{6}$$

2.2 Basic Principle

Here, $\boldsymbol{X} = \begin{bmatrix} x_1 & x_2 & x_3 \end{bmatrix}^{\mathrm{T}}$ represents the measurements of the magnetometer in engineering units, which are usually the engineering outputs of the current or voltage and are null-centered by

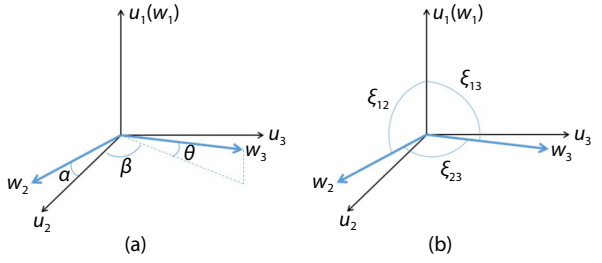

Figure 1. (a) Relationship between the coordinate systems $\boldsymbol{F}_w$ and $\boldsymbol{F}_u$. (b) Illustration of angles between the mechanical axes of the sensor.

the offset vector $\boldsymbol{O} = [\ O_1 \quad O_2 \quad O_3\ ]^{\mathrm{T}}$. After normalization with respect to the physical units (nT) with the sensitivities $\boldsymbol{S}$ (a diagonal matrix), the raw output values of the magnetometer $\boldsymbol{B}_m = [\ B_{m1} \quad B_{m2} \quad B_{m3}\ ]^{\mathrm{T}}$, in the coordinate system $\boldsymbol{F}_w$, can be expressed as

$$\boldsymbol{B}_m = \boldsymbol{S}(\boldsymbol{X} - \boldsymbol{O}). \tag{7}$$

Here, $\boldsymbol{B} = [\ B_1 \quad B_2 \quad B_3\ ]^{\mathrm{T}}$, represents the calibrated, ideal orthogonal magnetic fields in the coordinate system $\boldsymbol{F}_u$. According to Equation (2), we obtain the relationship between $\boldsymbol{B}$ and $\boldsymbol{B}_m$ expressed as Equation (8), which can be used as the mathematical description of the ground calibration:

$$\boldsymbol{B} = \boldsymbol{T}^{\mathrm{T}}\boldsymbol{B}_m = \boldsymbol{T}^{\mathrm{T}}\boldsymbol{S}(\boldsymbol{X} - \boldsymbol{O}) = \boldsymbol{M}(\boldsymbol{X} - \boldsymbol{O}). \tag{8}$$

In particular, offset vector $\boldsymbol{O}$ can be obtained directly if the external field is zero. And the calibration transfer matrix $\boldsymbol{M}$ is defined by

$$\boldsymbol{M} = \boldsymbol{T}^{\mathrm{T}}\boldsymbol{S}, \tag{9}$$

where

$$\boldsymbol{M} = \begin{bmatrix} m_{11} & m_{12} & m_{13} \\ m_{21} & m_{22} & m_{23} \\ m_{31} & m_{32} & m_{33} \end{bmatrix} = \begin{bmatrix} s_1 & s_2\cos\xi_{12} & s_3\cos\xi_{13} \\ 0 & s_2\sin\xi_{12} & s_3\dfrac{\cos\xi_{23} - \cos\xi_{12}\cos\xi_{13}}{\sin\xi_{12}} \\ 0 & 0 & s_3\sqrt{\sin^2\xi_{13} - \dfrac{(\cos\xi_{23} - \cos\xi_{12}\cos\xi_{13})^2}{\sin^2\xi_{12}}} \end{bmatrix},$$

where m_{ij} $(i, j = 1, 2, 3)$ represents the elements of $\boldsymbol{M}$.

For a vector calibration, several groups of vector magnetic field $\boldsymbol{B}$ are provided. The calibration transfer matrix $\boldsymbol{M}$ can be estimated from Equation (8) by using the least squares estimation method. The sensitivity $\boldsymbol{S} = \mathrm{diag}(s_1 \quad s_2 \quad s_3)$ and the matrix $\boldsymbol{T}^{\mathrm{T}}$ can then be expressed as follows:

$$\begin{aligned} s_1 &= m_{11}, \\ s_2 &= \sqrt{m_{12}^2 + m_{22}^2}, \\ s_3 &= \sqrt{m_{13}^2 + m_{23}^2 + m_{33}^2}. \end{aligned} \tag{10}$$

$$\boldsymbol{T}^{\mathrm{T}} = \begin{bmatrix} \dfrac{m_{11}}{s_1} & \dfrac{m_{12}}{s_2} & \dfrac{m_{13}}{s_3} \\ 0 & \dfrac{m_{22}}{s_2} & \dfrac{m_{23}}{s_3} \\ 0 & 0 & \dfrac{m_{33}}{s_3} \end{bmatrix}. \tag{11}$$

According to Equations (6) and (11), the misalignment angles between the sensor axes can be derived and expressed with the elements of calibration transfer matrix $\boldsymbol{M}$:

$$\begin{aligned} \xi_{12} &= \arccos\left(\frac{m_{12}}{\sqrt{m_{12}^2 + m_{22}^2}}\right), \\ \xi_{23} &= \arccos\left(\frac{m_{12}m_{13} + m_{22}m_{23}}{\sqrt{(m_{12}^2 + m_{22}^2)(m_{13}^2 + m_{23}^2 + m_{33}^2)}}\right), \\ \xi_{13} &= \arccos\left(\frac{m_{13}}{\sqrt{m_{13}^2 + m_{23}^2 + m_{33}^2}}\right). \end{aligned} \tag{12}$$

Therefore, all the calibration parameters of the magnetometer could be determined.

3. Calibration of the MOMAG Sensors

3.1 MOMAG Sensor and Calibration Facilities

The MOMAG sensor consists of ring cores, coil systems, and support and housing configurations. Two orthogonal intertwined ring cores of different sizes are integrated into the three-dimensional Helmholtz coil systems, as presented in Figure 2. The sensors are mounted on a more than 3-m-long deployable boom. Although the sensors are protected by multilayer insulation blankets to reduce thermal gradients, they will still experience temperature changes in orbit. (The temperature in orbit cam vary from −120°C to +5°C for the FGM sensors and from −40°C to +50°C for the electronics.)

The ground calibration experiments of sensitivities, misalignment angles, and their dependencies on temperature change for the MOMAG sensors were performed at the Magnetsrode coil facility in Braunschweig, Germany. At this facility, the magnetometers can be operated in calibrated and stable magnetic field conditions. Artificial magnetic calibration fields can be applied in a range from −100,000 to +100,000 nT on each individual coil axis within a homogenous field volume (<1 nT variation) of 20 × 20 × 20 cm (Risbo et al., 2003). In addition to the DC fields, AC fields can be applied in the same range, with frequencies up to the order of kilohertz. The device under test can be operated not only at room temperature but also in a wide temperature range by using a specially designed nonmagnetic thermal box.

During MOMAG calibration, the temperature range is somehow constrained and the sensor is exposed to the external magnetic field variance in the coil facility. The calibration of offsets for the MOMAG sensors and their dependencies on temperature change were conducted in the low-temperature test facility at the Magnetometer Laboratory of IWF (Graz). The facility consists of the following main parts: a three-layer magnetic shielding set, low-temperature equipment, and a control system. Because the temperature equipment is packed into the magnetic shielding set, external influences have no effect on the sensor offset measurements, and the calibration of magnetometer offsets within a temperature range from −150°C to +150°C is available. In the facility, the weakest residual field caused by both the facility and the external field is less than 1 nT in the horizontal direction and

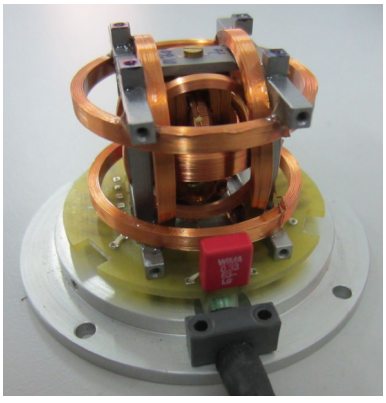

Figure 2. Configuration of the fluxgate magnetometer sensor.

approximately 2 nT in the vertical direction. The sensor under test can be rotated by a Teflon pipe for an accurate offset measurement during the full temperature cycle. The coil system and the low-temperature test facility are presented in Figure 3.

3.2 Calibration of Sensor Sensitivities and Misalignment Angles

During the calibration, the sensor was mounted in the thermal box at the center of the coil facility and kept stationary, as shown in Figure 4. The desired magnetic fields were controlled automatically by a computer program. The fields were generated by the three axes of the coil system, in turn varying from −10,000 to 10,000 nT with a step of 1,000nT. A total of 63 magnetic field vectors were obtained to ensure enough data were collected to determine the six calibration parameters in the matrix $\boldsymbol{M}$ by the least squares estimation method. Each coil field setting was maintained for approximately 23 s, and the vector samples were logged by the sensor at a 1 Hz sampling rate. A typical response of the FGM sensor to the orthogonal coil field vectors $\boldsymbol{B}$ is presented in Figure 5.

The calibration experiments were also conducted at different temperature points to determine the temperature dependencies of the sensitivities and misalignment angles. The temperature-dependent sensitivity $s_i(T)$ and temperature-dependent misalignment angle $\xi_{ij}(T)$ can be expressed as follows:

$$\begin{aligned} s_i(T) &= \sum_{k=0}^{n} s_{k,i} T^k, \\ \xi_{ij}(T) &= \sum_{k=0}^{n} \xi_{k,ij} T^k. \end{aligned} \tag{13}$$

in which $i, j = 1, 2, 3$ represent the sensor axes.

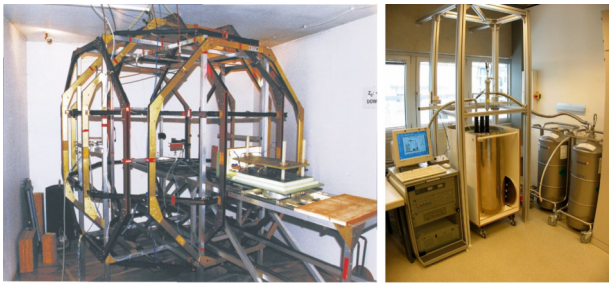

(a) (b)

Figure 3. Ground calibration facilities of the Mars orbiter magnetometer. (a) The Magnetsrode coil facility in Braunschweig, Germany. (b) The sensor offset calibration facility in Graz, Austria.

Figure 4. The Mars orbiter magnetometer sensor fixed at a mounting plate and ready to be pushed into the thermal box.

The temperature dependencies of the sensitivities and misalignment angles for the FGM sensors are presented in Figure 6. Results of the coefficient fitting of Equation (13) are listed in Table 2 and 3. The order of the primary term coefficients was only −5, and the order of the secondary term coefficients was much smaller, which means that both the sensitivity of each sensor axis and the misalignment angles between the sensor axes were quite stable in response to the temperature change and that no clear temperature dependency signatures could be seen.

3.3 Calibration of Sensor Offsets

A more accurate method uses the usual sensor rotations by 180° around two main axes to obtain the sensor offsets. At a certain temperature point, the sensor was mounted on the tip of the Teflon pipe and kept stationary in the facility, with one axis along the vertical direction and the other two axes along the horizontal direction. The magnetic field data $B_i(0°)$ along the rotation axis were obtained. By rotating the pipe 180°, other magnetic field data $B_i(180°)$ were also recorded. The sensor offsets O_i in the two axes and the residual field B_r along the horizontal direction in the facility can then be derived by adding the measurement values from the normal and turned positions:

$$\begin{aligned} O_i &= \frac{B_i(0^\circ) + B_i(180^\circ)}{2}, \\ B_r &= \frac{B_i(0^\circ) - B_i(180^\circ)}{2}. \end{aligned} \tag{14}$$

All the sensor offsets could be obtained by changing the sensor axis along the vertical direction and repeating the procedure described above. Furthermore, four discrete temperature points (27°C, −19°C, −70°C, −124°C) were set for calibrating the temperature dependencies of the sensor offsets. Each temperature point was maintained for no less than 5 minutes before rotating the

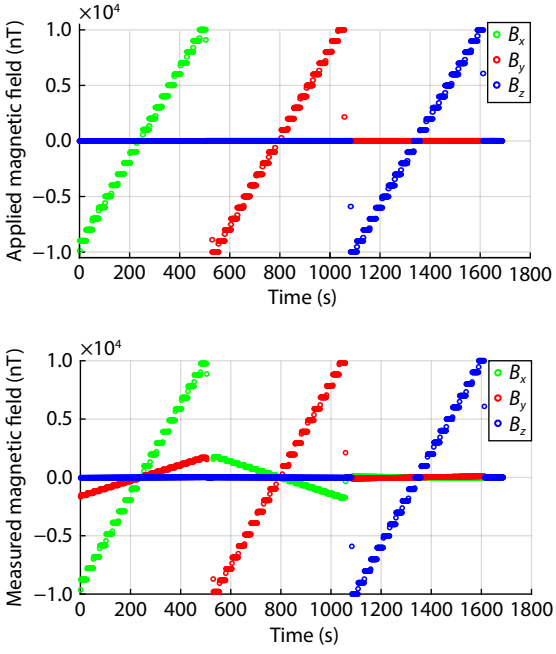

Figure 5. Response of the sensor to the orthogonal coil field vectors $\boldsymbol{B}$. (Top panel) The magnetic field applied by the coil system. (Bottom panel) The magnetic field data recorded by the sensor.

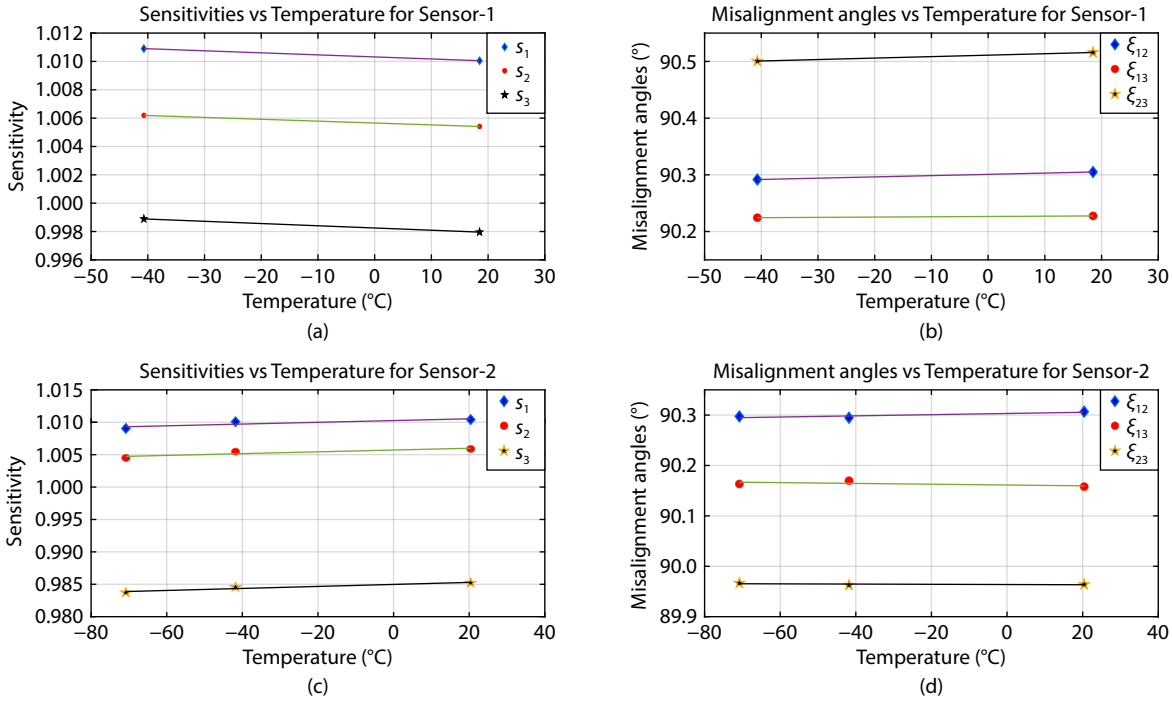

Figure 6. Temperature dependencies of the sensitivity and misalignment angles for the Mars orbiter magnetometer sensors. (a) The temperature dependence of the sensitivity for Sensor-1. (b) The temperature dependence of the misalignment angles for Sensor-1. (c) The temperature dependence of the sensitivity for Sensor-2. (d) The temperature dependence of the misalignment angles for Sensor-2.

Table 2. Temperature coefficients of sensitivity.

Sensor	Sensitivity	$s_{0,i}$	$s_{1,i}$	$s_{2,i}$
Sensor-1	s_1	1.0103	−1.44e-5	—
	s_2	1.0057	−1.32e-5	—
	s_3	0.9982	−1.57e-8	—
Sensor-2	s_1	1.0093	−2.07e-5	−9.38e-8
	s_2	1.0049	−1.45e-5	−9.61e-9
	s_3	0.9840	−2.09e-5	−6.37e-8

Table 3. Temperature coefficients of the misalignment angles.

Sensor	Misalignment angle	$\xi_{0,ij}$	$\xi_{1,ij}$	$\xi_{2,ij}$
Sensor-1	ξ_{12}	90.30	2.25e-4	—
	ξ_{13}	90.23	5.16e-5	—
	ξ_{23}	89.51	2.58e-5	—
Sensor-2	ξ_{12}	89.96	−3.82e-5	5.12e-7
	ξ_{13}	90.17	−6.66e-5	−3.74e-6
	ξ_{23}	90.29	6.52e-5	3.05e-6

sensor, and magnetic field samples were logged by the sensor at a 1 Hz sampling rate. A typical calibration procedure is presented in Figure 7.

The offset of each sensor axis versus the temperature change is presented in Figure 8, and the peak-to-peak values of the offset drift are listed in Table 4. The stability of the MOMAG sensor offset drift was less than 0.01 nT/°C, showing a stable offset for accurate measurement during a temperature change in orbit.

We also calibrated and discussed the dependence of the sensor offset on the temperature change of the electronics during the MOMAG ground calibration. The sensors were placed in the magnetic shielding facility and the electronics were placed into the thermal chamber with a continuous temperature change from −40°C to +50°C. Table 5 provides a summary of the dependence of the sensor offset on the temperature change of the electronics. The largest sensor offset drift was less than 0.95 nT, showing that the sensor offset was insensitive to the temperature change of the electronics.

4. Summary and Conclusions

The ground calibration of the MOMAG sensors is essential before instrument delivery for accurate magnetic measurements in orbit. Calibration experiments of sensor sensitivities, misalignment angles, offsets, and their dependencies on temperature change were conducted at the Magnetsrode coil facility in Braunschweig, Germany and the low-temperature test facility in Graz, Austria. The calibration results showed that the sensitivities and misalignment angles of the FGM sensors were constructed as second-order polynomials with respect to temperature. The order of the primary term coefficients was only −5, and the order of the secondary term coefficients was even smaller, meaning that the effect of temperature on the sensitivity and misalignment angle between axes was negligible. The offsets were determined by the rotation method in the low-temperature test facility. The stability of the sensor offset over temperature was tested at four temperature points (27°C, −19°C, −70°C, −124°C), and the stability of the sensor offset drift was less than 0.01 nT/°C, demonstrating that

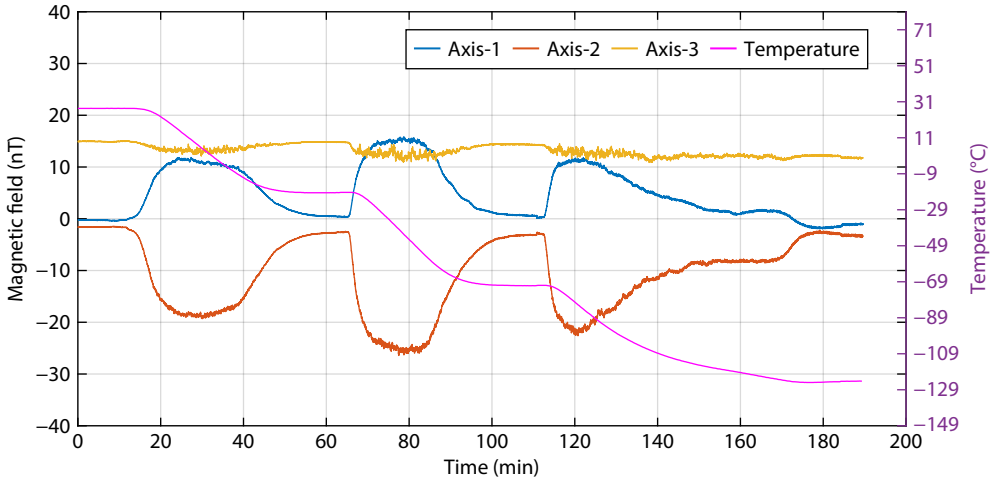

Figure 7. A typical calibration procedure of the sensor offset stability. (Axis-3 is the rotation axis.)

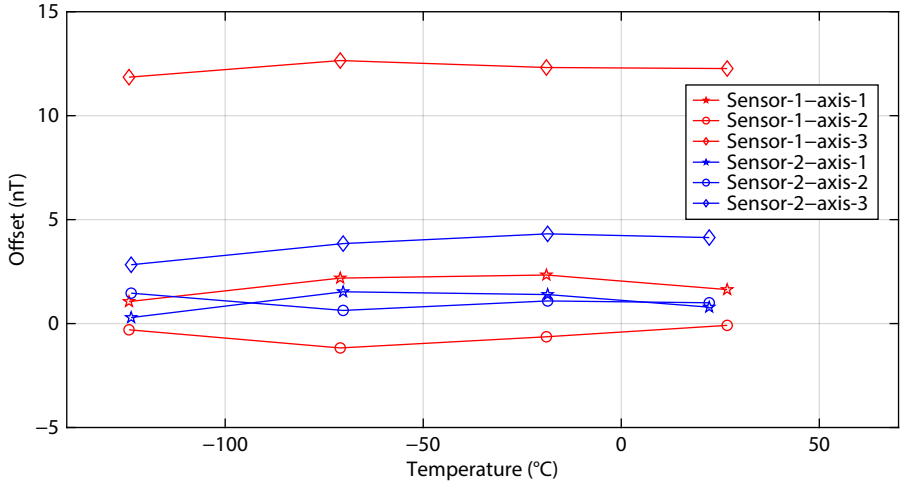

Figure 8. Offset values of the Mars orbiter magnetometer sensors in each axis versus the temperature change.

Table 4. Peak-to-peak values of the offset drift for each of the Mars orbiter magnetometer sensors.

Sensor	Offset drift (nT)		
	Axis-1	Axis-2	Axis-3
Sensor-1	1.28	1.08	0.77
Sensor-2	1.24	0.83	1.49

Table 5. Dependence of the sensor offset on the temperature change of the electronics.

Sensor	Electronics	Temperature (°C)		Offset drift (nT)		
		Lowest	Highest	Axis-1	Axis-2	Axis-3
Sensor-1	Electronic-1	−39.4	48.2	0.22	0.01	0.32
Sensor-2	Electronic-2	−35.6	50.9	0.27	0.44	0.95

the sensor offset is stable enough for the Mars exploration mission.

Acknowledgments

This work was financially supported by the Chinese National Space Administration (CNSA), the Strategic Priority Program (Grant No. XDB41000000), the Key Research Program of Frontier Sciences (No. QYZDB-SSW-DQC015), and the Strategic Priority Program (Grant No. XDB41030100) of the Chinese Academy of Sciences. Thanks are extended to the entire MOMAG team at the University of Science and Technology of China.

References

Acuña, M. H. (2002). Space-based magnetometers. *Rev. Sci. Instrum.*, *73*(11), 3717–3736. https://doi.org/10.1063/1.1510570

Auster, H. U., Fornacon, K. H., Georgescu, E., Glassmeier, K. H., and Motschmann, U. (2002). Calibration of flux-gate magnetometers using relative motion. *Meas. Sci. Technol.*, *13*(7), 1124–1131. https://doi.org/10.1088/0957-0233/13/7/321

Auster, H. U., Glassmeier K. H., Magnes W., Aydogar O., Baumjohann W., Constantinescu D., Fischer D., Fornacon K. H., Georgescu E., … Wiedemann, K. (2008). The THEMIS fluxgate magnetometer. *Space Sci. Rev.*, *141*(1–4), 235–264. https://doi.org/10.1007/s11214-008-9365-9

Cheng, B. J., Zhou, B., Magnes, W., Lammegger, R., and Pollinger, A. (2018). High precision magnetometer for geomagnetic exploration onboard of the China Seismo-Electromagnetic Satellite. *Sci. China Technol. Sci.*, *61*(5), 659–668. https://doi.org/10.1007/s11431-018-9247-6

Cheng, S. N., Wang, G. Q., Pan, Z. H., Meng, L. F., Yi, Z., and Zhang, T. L. (2022). An optimal method for in-flight calibration of the fluxgate magnetometer

when the total magnetic field of Alfvén waves has a drift trend. *Chinese J. Geophys.* (*in Chinese*), *65*(5), 1558–1570. https://doi.org/10.6038/cjg2022P0362

Hu, X. W., Wang, G. Q., and Pan, Z. H. (2022a). Automatic calculation of the magnetometer zero offset using the interplanetary magnetic field based on the Wang–Pan method. *Earth Planet. Phys.*, *6*(1), 52–60. https://doi.org/10.26464/epp2022017

Hu, X. W., Wang, G. Q., Pan, Z. H., and Zhang, T. L. (2022b). Application of the Wang–Pan method based on mirror mode structures on the in-flight calibration of magnetometers. *Chinese J. Geophys.* (*in Chinese*), *65*(6), 1940–1950. https://doi.org/10.6038/cjg2022P0640

Li, C. L., Liu, J. J., Geng, Y., Cao, J. B., Zhang, T. L., Fang, G. Y., Yang, J. F., Shu, R., Zou, Y. L., … Ouyang, Z. Y. (2018). Scientific objectives and payload configuration of China's first Mars exploration mission. *J. Deep Space Explor.* (*in Chinese*), *5*(5), 406–413. https://doi.org/10.15982/j.issn.2095-7777.2018.05.002

Li, C. L., Zhang, R. Q., Yu, D. Y., Dong, G. L., Liu, J. J., Geng, Y., Sun, Z. Z., Yan, W., Ren, X., and Su, Y. (2021). China's Mars exploration mission and science investigation. *Space Sci. Rev.*, *217*(4), 57. https://doi.org/10.1007/s11214-021-00832-9

Liu, K., Hao, X. J., Li, Y. R., Zhang, T. L., Pan, Z. H., Chen, M. M., Hu, X. W., Li, X., Shen, C. L., and Wang, Y. M. (2020). Mars orbiter magnetometer of China's first Mars mission Tianwen-1. *Earth Planet Phys.*, *4*(4), 384–389. https://doi.org/10.26464/epp2020058

Magnes, W., Berghofer, G., Mocnik, K., Koren, W., Schwingenschuh, K., Stachel, M., Jernej, I., Riedler, W., Russell, C. T., … Beek, T. J. (1998). A spaceborne magnetometer tested under extended temperature conditions (experiment MAREMF-OS/MARS-96). *Meas. Sci. Technol.*, *9*(8), 1219–1228. https://doi.org/10.1088/0957-0233/9/8/013

Nielsen, O. V., Petersen, J. R., Primdahl, F., Brauer, P., Hernando, B., Fernandez, A., Merayo, J. M. G., and Ripka, P. (1995). Development, construction and analysis of the 'Ørsted' fluxgate magnetometer. *Meas. Sci. Technol.*, *6*(8), 1099–1115. https://doi.org/10.1088/0957-0233/6/8/004

Risbo, T., Brauer, P., Merayo, J. M. G., Nielsen, O. V., Petersen, J. R., Primdahl, F., and Richter, I. (2003). Ørsted pre-flight magnetometer calibration mission. *Meas. Sci. Technol.*, *14*(5), 674–688. https://doi.org/10.1088/0957-0233/14/5/319

Russell, C. T., Anderson, B. J., Baumjohann, W., Bromund, K. R., Dearborn, D., Fischer, D., Le, G., Leinweber, H. K., Leneman, D., … Richter, I. (2016). The magnetospheric multiscale magnetometers. *Space Sci. Rev.*, *199*(1–4), 189–256. https://doi.org/10.1007/s11214-014-0057-3

Shimizu, H., Takahashi, F., Horii, N., Matsuoka, A., Matsushima, M., Shibuya, H., and Tsunakawa, H. (2008). Ground calibration of the high-sensitivity SELENE lunar magnetometer LMAG. *Earth Planets Space*, *60*(4), 353–363. https://doi.org/10.1186/bf03352800

Wang, G. Q., and Pan, Z. H. (2021a). A new method to calculate the fluxgate magnetometer offset in the interplanetary magnetic field: 1. Using Alfvén waves. *J. Geophys. Res.: Space Phys.*, *126*(4), e2020JA028893. https://doi.org/10.1029/2020ja028893

Wang, G. Q., and Pan, Z. H. (2021b). A new method to calculate the fluxgate magnetometer offset in the interplanetary magnetic field: 2. Using mirror mode structures. *J. Geophys. Res.: Space Phys.*, *126*(9), e2021JA029781. https://doi.org/10.1029/2021ja029781

Wang, G. Q. (2022). High-precision calibration of the fluxgate magnetometer offset vector in the terrestrial magnetosheath. *Astrophys. J.*, *929*(1), 87. https://doi.org/10.3847/1538-4357/ac5907

Wang, G. Q., and Pan, Z. H. (2022). Fluxgate magnetometer offset vector determination using current sheets in the solar wind. *Astrophys. J.*, *926*(1), 12. https://doi.org/10.3847/1538-4357/ac3d8f

Yamamoto, T., Kokubun, S., and GEOTAIL/PLANET-B MGF Team. (1996). Ground calibration of high-sensitivity magnetometers for spacecraft use. *Uchu Kagaku Kenkyuusho Houkoku*(88), 1–24.